

The H I Gas Disk Thickness of the Ultra-diffuse Galaxy AGC 242019

Xin Li,¹ Yong Shi,^{1,2*} Zhi-Yu Zhang,^{1,2} Jianhang Chen,³ Xiaoling Yu,¹ Junzhi Wang,⁴ Qiusheng Gu^{1,2} and Songlin Li^{5,6}

¹*School of Astronomy and Space Science, Nanjing University, Nanjing 210093, People's Republic of China*

²*Key Laboratory of Modern Astronomy and Astrophysics (Nanjing University), Ministry of Education, Nanjing 210093, People's Republic of China*

³*European Southern Observatory, Karl-Schwarzschild-Strasse 2, D-85748 Garching bei Muenchen, Germany*

⁴*Shanghai Astronomical Observatory, Chinese Academy of Sciences, 80 Nandan Road, Shanghai 200030, People's Republic of China*

⁵*Research School of Astronomy and Astrophysics, Australian National University, Canberra, ACT 2611, Australia*

⁶*ARC Centre of Excellence for All Sky Astrophysics in 3 Dimensions (ASTRO 3D), Australia*

Accepted XXX. Received YYY; in original form ZZZ

ABSTRACT

Ultra-diffuse galaxies (UDGs) are as faint as dwarf galaxies but whose sizes are similar to those of spiral galaxies. A variety of formation mechanisms have been proposed, some of which could result in different disk thicknesses. In this study, we measure the radial profile of the H I scale height (h_g) and flaring angle (h_g/R) of AGC 242019 through the joint Poisson-Boltzmann equation based on its well spatially-resolved HI gas maps. The mean H I scale height of AGC 242019 is $\langle h_g \rangle \approx 537.15 \pm 89.4$ pc, and the mean flaring angle is $\langle h_g/R \rangle \approx 0.19 \pm 0.03$. As a comparison, we also derive the disk thickness for a sample of 14 dwarf irregulars. It is found that the H I disk of AGC 242019 has comparable thickness to dwarfs. This suggests that AGC 242019 is unlikely to experience much stronger stellar feedback than dwarf galaxies, which otherwise leads to a thicker disk for this galaxy.

Key words: galaxies: ISM – galaxies: kinematics and dynamics – galaxies: dwarf – galaxies: structure.

1 INTRODUCTION

Ultra-diffuse galaxies (UDGs) are characterized as faint but extended objects. Their central surface brightness is fainter than 24 mag/arcsec² while the effective radius in the optical is larger than 1.5 kpc (van Dokkum et al. 2015). They have been found in a wide range of environments. UDGs in galaxy clusters are red and round with negligible star formation (van Dokkum et al. 2015, 2016). Some UDGs in the clusters are suggested to be failed L_* galaxies, such as Dragonfly 44 because of its abundant global clusters, high internal velocity dispersion, and massive host halo. Some other cluster UDGs are instead lacking of dark matter such as NGC1052-DF2 and NGC1052-DF4 (van Dokkum et al. 2018, 2019). These objects may lose a large fraction of baryons and dark matter by tidal interactions/stripping. In contrast to the cluster UDGs, UDGs in the field are gas rich with mild star formation (Leisman et al. 2017). They likely reside in dwarf-size halos as indicated by their kinematic data (Shi et al. 2021; Mancera Piña et al. 2022).

To further understand what mechanism regulates the UDG formation, it is important to characterize the disk thickness of UDGs. As suggested by Chan et al. (2018), the field UDGs with high spins tend to be more disky, while those in normal spin halos are puffier. Di Cintio et al. (2017) pointed out that episodic stellar wind generated by bursty star formation can enlarge and puff the disk of dwarf galaxies to produce UDGs. Cluster UDGs are more prolate and spheroidal

(e.g. Burkert 2017; Chan et al. 2018; Jiang et al. 2019; Liao et al. 2019), and the thickness of their progenitors depends on their evolutionary channels. For example, progenitors of cluster UDGs with disks may become spheroidal throughout the tidal stirring (Chan et al. 2018; Rong et al. 2020) or stellar feedback (e.g. Sánchez-Janssen et al. 2010; Liao et al. 2019; Bacchini et al. 2020), while thicker and more prolate progenitors are formed by quenching their star formation through the ram-pressure stripping (Chan et al. 2018).

For the gas-rich UDG, it is possible to estimate the thickness of gaseous disks through gas kinematic observations. As gas is collisional, shapes of gaseous disks are sensitive to galactic activities such as the gravity instability, stellar feedback, galaxy interaction, etc. (e.g. Scannapieco et al. 2008; Marinacci et al. 2017). Here we quantify the thickness as the scale height, defined as the distance to the mid-plane whose volume density is half of the maximum along the vertical direction of the disk, and derive it theoretically based on vertical hydrostatic equilibrium. In a self-gravitating system, the disk stability is determined by gravity and pressure of vertical velocity dispersion (Narayan & Jog 2002a,b). By adopting Poisson's equation that describes the gravitational potential of galaxies, several works estimated the scale height of spiral and dwarf galaxies with different approximations and assumptions (e.g. Narayan & Jog 2002a; Banerjee et al. 2011; Banerjee & Jog 2013; Patra 2019; Sarkar & Jog 2019; Patra 2020; Das et al. 2020). However, these methods require high spatial-resolution observational data.

We focus on the H I disk of AGC 242019 whose major axis is resolved into 14 beams with a beam size of $9.''85 \times 9.''33$ (Shi et al.

* E-mail: yong@nju.edu.cn

2021), which makes it possible to obtain the reliable estimate of its H I disk height. The object has $M_{\text{HI}} = (8.51 \pm 0.36) \times 10^8 M_{\odot}$ and $M_{*} = (1.37 \pm 0.05) \times 10^8 M_{\odot}$. In § 2, we describe our methods and input parameters that we used to derive the scale height of the H I disk. In § 3, we show the results of the H I scale height of AGC 242019. We compare the H I scale height and flaring angle of our target with those of dwarf irregulars, and discuss these results in § 4.

2 METHODS

Atomic gas and stars are modeled as two axis-symmetric disks, while molecular gas is estimated to be negligible in this galaxy (Shi et al. 2021). These two components are further assumed to be co-planar and co-center with their host dark matter halo. The disks are assumed to be isothermal with each component satisfying hydrostatic equilibrium in the vertical direction.

2.1 Joint Poisson-Boltzmann equation

We adopt a joint Poisson-Boltzmann equation (Banerjee & Jog 2013; Patra 2019; Sarkar & Jog 2019; Patra 2020) for the star and gas components at a radius R in a cylindrical coordinate as:

$$\langle \sigma_z \rangle_i^2 \frac{\partial}{\partial z} \left(\frac{1}{\rho_i} \frac{\partial \rho_i}{\partial z} \right) = -4\pi G(\rho_g + \rho_* + \rho_{\text{DM}}) + \frac{1}{R} \frac{\partial}{\partial R} \left(R \frac{\partial \Phi_{\text{tot}}}{\partial R} \right), \quad (1)$$

$$\left(R \frac{\partial \Phi_{\text{tot}}}{\partial R} \right)_{R,z} = (v_{\text{rot}}^2)_{R,z}. \quad (2)$$

This equation is the combination of the vertical hydrostatic equilibrium equation given as $\frac{\partial}{\partial z}(\rho_i \langle \sigma_z^2 \rangle_i) + \rho_i \frac{\partial \Phi_{\text{tot}}}{\partial z} = 0$, and Poisson's equation that describes the gravitational potential of a galaxy as $\frac{\partial^2 \Phi_{\text{tot}}}{\partial z^2} + \frac{1}{R} \frac{\partial}{\partial R} \left(R \frac{\partial \Phi_{\text{tot}}}{\partial R} \right) = 4\pi G(\rho_g + \rho_* + \rho_{\text{DM}})$, where i denotes either stars or H I components, $\langle \sigma_z \rangle_i$ is the vertical velocity dispersion and is independent of z under the assumption of isothermal disks (van der Kruit 1981), G is gravitational constant, ρ_g is the gas volume density, ρ_* is the stellar volume density, ρ_{DM} is the dark matter volume density which is a function of both R and z . The total gravitational potential Φ_{tot} includes stars, gas and dark matter, and its radial gradient is measured through the rotation curve independent of z (see Banerjee et al. 2011, for more details). Some studies do not consider $\partial \Phi_{\text{tot}} / \partial R$ for spiral galaxies at the flat part of the rotation curve where the radial gradient becomes negligible (e.g. Narayan & Jog 2002a; Das et al. 2020).

2.2 Input parameters

The input parameters to solve the above equations are: (1) the radial profile of the H I surface density Σ_g ; (2) the radial profile of the H I velocity dispersion $\langle \sigma_z \rangle_g$; (3) the circular velocity v_{rot} as a function of radius; (4) the radial profile of stellar mass surface density Σ_* ; (5) the radial profile of the stellar velocity dispersion $\langle \sigma_z \rangle_*$; (6) the radial profile of the dark matter density ρ_{DM} .

For AGC 242019, measurements of these parameters are detailed in Shi et al. (2021) except for $\langle \sigma_z \rangle_*$ that is present at the end of the section. The first three were based on the H I data that was acquired through the Very Large Array (VLA) with a velocity resolution of $\sim 7 \text{ km s}^{-1}$ and a beam size of $9.''85 \times 9.''33$. The stellar surface density profile Σ_* was obtained from $3.6 \mu\text{m}$ broad band image of Wide-field

Infrared Survey Explorer (WISE) (Wright et al. 2010) with Kroupa initial mass function (IMF) and the mass-to-light ratio of $\gamma_{3.6 \mu\text{m}} = 0.6$. We fit Σ_* with a Sérsic profile, $\Sigma_*(R) = \Sigma_{*,0} \exp \left[-(R/R_d)^{1/n} \right]$ (Graham & Driver 2005, equation (14)), to get the disk scale length $R_d = 4.95 \text{ kpc}$. The radial profile of the dark matter density is well fitted by a Navarro-Frenk-White model (NFW, Navarro et al. 1997):

$$\rho_{\text{DM}}(R, z) = \frac{\rho_c \delta_{\text{char}}}{\left(\frac{\sqrt{R^2+z^2}}{R_s} \right) \left(1 + \frac{\sqrt{R^2+z^2}}{R_s} \right)^2}, \quad (3)$$

where ρ_c is the present critical density, $\delta_{\text{char}} = \frac{200c^3 g}{3}$, $g = \frac{1}{\ln(1+c) - c/(1+c)}$, $c = R_{200}/R_s$. As derived in Shi et al. (2021), the scale radius R_s is $33.3 \pm 9.1 \text{ kpc}$ and R_{200} is $65.0 \pm 7.4 \text{ kpc}$. The radial profiles of the remaining five parameters are listed in Table 1.

For dwarf irregulars as a comparison to AGC 242019, we carry out similar calculations for a sample of 14 objects as listed in Table 2. Their radial profiles of the HI surface density, velocity dispersion, and circular velocity were derived by Iorio et al. (2017) based on the H I data of the LITTLE THINGS project (Hunter et al. 2012). Their stellar mass surface density radial profiles were given by Zhang et al. (2012), for which we fit the same Sérsic profile to get their scale lengths (R_d). To obtain the rotation curve of dark matter, we first run the ROTMOD task from GIPSY (Begeman 1989) to estimate the rotation curves of stellar and gas components, and then subtract them from the observed rotation curve. As Oh et al. (2015) showed that the dark matter profiles of these irregulars can be described by pseudo-isothermal (ISO) models (Begeman et al. 1991), we then fit the rotation curve to obtain the radial profiles of dark matter density through ISO models:

$$\rho_{\text{DM}}(R, z) = \frac{\rho_0}{1 + \frac{R^2+z^2}{R_c^2}}, \quad (4)$$

where ρ_0 is the central density, and R_c is the core radius of the halo. We note that our results change little if adopting the NFW profile (Patra 2020). Some dwarf irregulars can have bar structures or active star formation (e.g. Hunter & Elmegreen 2006; Hunter et al. 2011; Zhang et al. 2012; Johnson et al. 2015; Iorio et al. 2017; Patra & Jog 2019). Since bars or violent star formation may induce non-circular motion to break the hydrostatic equilibrium assumption (Johnson et al. 2015; Iorio et al. 2017; Patra & Jog 2019), we exclude radial regions of optical bars for WLM, DDO 154, NGC 2366, DDO 126, and DDO 133 (e.g. Hunter & Elmegreen 2006; Hunter et al. 2011; Zhang et al. 2012), as well as the radial region of the H I bar for DDO 164 (Johnson et al. 2015; Iorio et al. 2017; Patra & Jog 2019). The derived disk scale lengths, parameters of dark matter models and adopted bar radii are listed in Table 2.

For both AGC 242019 and the comparison dwarfs, it is extremely difficult to measure the stellar velocity dispersion as a function of radius. As a result we adopt the radial profile of the stellar vertical dispersion proposed by e.g. van der Kruit & Searle (1981a): $\langle \sigma_z \rangle_*(r) = \langle \sigma_z \rangle_{*,0} \exp(-r/2R_d)$, where $\langle \sigma_z \rangle_{*,0}$ is the central stellar velocity dispersion. The simplified hydrostatic equilibrium with the isothermal stellar disk gives $\langle \sigma_z \rangle_{*,0} = \sqrt{2\pi G \Sigma_* z_e}$, where z_e is defined for the stellar vertical density profile $\rho_z(z) = \text{sech}^2\left(\frac{z}{2z_e}\right)$ (see van der Kruit 1988, for more details). By fitting the vertical brightness distributions of 33 edge-on spiral galaxies in Kregel et al. (2002) with $\text{sech}^2\left(\frac{z}{2z_e}\right)$ profiles, we derive $z_e \sim R_d/9.5$. We note that although such estimates of the stellar velocity dispersion can have large uncertainties, we will show later that the adopted $\langle \sigma_z \rangle_*$ have no significant effects on the H I scale heights.

Table 1. Radial profiles of different physical parameters of AGC 242019.

R (kpc)	Σ_g ($M_\odot \text{ pc}^{-2}$)	$\langle \sigma_z \rangle_g$ (km s^{-1})	v_{rot} (km s^{-1})	Σ_* ($M_\odot \text{ pc}^{-2}$)	$\langle \sigma_z \rangle_*$ (km s^{-1})	h_g (pc)
(1)	(2)	(3)	(4)	(5)	(6)	(7)
0.67	2.78 ± 0.130	4.5 ± 1.3	10.4 ± 1.2	1.90 ± 0.049	4.84	183.68 ± 69.97
2.02	3.07 ± 0.092	7.7 ± 1.3	14.5 ± 1.3	1.79 ± 0.030	4.22	465.80 ± 116.28
3.36	2.94 ± 0.063	7.7 ± 1.0	22.3 ± 1.4	1.40 ± 0.028	3.69	549.60 ± 109.77
4.71	2.83 ± 0.052	7.0 ± 1.6	29.4 ± 1.8	0.81 ± 0.026	3.22	633.88 ± 233.30
6.06	2.73 ± 0.045	6.5 ± 1.6	33.8 ± 1.6	0.30 ± 0.041	2.81	852.79 ± 338.98

(1) the radius to galactic center in kpc; (2) the gas mass surface density in $M_\odot \text{ pc}^{-2}$; (3) the H I vertical velocity dispersion in km s^{-1} ; (4) the circular velocity in km s^{-1} ; (5) the stellar mass surface density in $M_\odot \text{ pc}^{-2}$; (6) the stellar vertical velocity dispersion in km s^{-1} (see main text for details); (7) the H I scale height in pc (see main text for details). All data in columns (1)-(5) are obtained from Shi et al. (2021).

Table 2. Derived properties of dwarf irregulars.

Galaxy	R_d (kpc)	R_{bar} (kpc)	ρ_0 ($M_\odot \text{ pc}^{-3}$)	R_c (kpc)	$\langle \sigma_z \rangle_{*,0}$ (km s^{-1})	$\langle h_g \rangle_R$ (pc)	$\langle h_g \rangle_{R/R_d}$ (pc)
(1)	(2)	(3)	(4)	(5)	(6)	(7)	(8)
DDO 101	0.61		0.452 ± 0.075	0.455 ± 0.052	6.53	80.93 ± 13.10	57.55 ± 14.25
WLM	1.24	1.00 ^a	0.042 ± 0.006	1.046 ± 0.139	2.15	474.64 ± 39.16	317.89 ± 44.99
DDO 50	1.49		0.198 ± 0.091	0.351 ± 0.099	9.06	474.12 ± 45.85	215.87 ± 31.39
DDO 87	1.85		0.037 ± 0.012	1.283 ± 0.380	3.21	437.46 ± 50.45	244.22 ± 40.06
CVnldwA	1.23		0.016 ± 0.020	0.955 ± 0.368	1.78	252.50 ± 45.88	263.61 ± 35.26
DDO 52	1.11		0.030 ± 0.010	1.494 ± 0.366	4.61	455.63 ± 52.30	176.78 ± 54.30
UGC 8508	0.54		0.095 ± 0.040	0.705 ± 0.332	2.81	297.04 ± 46.48	233.57 ± 37.47
DDO 168	1.72	1.00 ^b	0.030 ± 0.006	1.943 ± 0.420	4.71	464.04 ± 45.24	467.66 ± 82.87
DDO 154	0.93	1.13 ^a	0.041 ± 0.005	1.134 ± 0.093	2.12	715.22 ± 41.08	
NGC 2366	2.93	4.00 ^a	0.022 ± 0.003	2.033 ± 0.264	2.34	751.22 ± 91.40	
DDO 126	1.47	0.97 ^a	0.019 ± 0.005	1.736 ± 0.504	2.20	564.00 ± 52.25	642.19 ± 66.51
DDO 133	1.14	1.48 ^a	0.088 ± 0.022	0.813 ± 0.168	3.89	355.93 ± 51.78	
DDO 216	0.93		0.041 ± 0.023	0.427 ± 0.176	2.56	335.42 ± 51.27	230.26 ± 25.04
DDO 53	1.70		0.049 ± 0.023	0.528 ± 0.155	1.86	386.41 ± 65.62	215.00 ± 26.30

Columns: (1) names of dwarf irregulars; (2) the disk scale length in kpc; (3) the bar length in kpc; (4) the central density of dark matter in $M_\odot \text{ pc}^{-3}$; (5) the core radius of dark matter halo in kpc; (6) the central stellar vertical velocity dispersion in km s^{-1} ; (7) the mean H I scale height ($0.67 < R < 6.06$ kpc) in pc; (8) the mean H I scale height ($0.1R_d < R < 1.2R_d$) in pc.

Notes. ^a Data obtained from Hunter & Elmegreen (2006); ^b Data obtained from Patra & Jog (2019).

2.3 Solving the equation

To help numerically solve the Poisson-Boltzmann equation, we further fit the rotation curves of dwarf irregulars with the Brandt profiles (Brandt 1960) to obtain the gradient. For those whose rotation curves do not reach the flat stages linear functions were adopted (see Patra 2019, 2020, for more details). Such fitting can also smooth the small fluctuation of the rotation curve to avoid the rapid change in the radial gradient.

Equation (1) is a bivariate second-order partial differential equation with two variables ρ_* and ρ_g . We adopt the same solving process as done in Banerjee et al. (2011), Patra (2019), Sarkar & Jog (2019) and Patra (2020). The python package `scipy` can solve equation (1) numerically with the 8-order Runge-Kutta method, and we can get both H I and stellar vertical profile at a given radius simultaneously. We set the initial conditions as $(\rho_i)_{z=0} = \rho_{i,0}$ and $\frac{d\rho_i}{dz}|_{z=0} = 0$, where $\rho_{i,0}$ is volume density at mid-plane. At first, we need to put a trial $\rho_{i,0}$, then iteratively solve the equation until the solved ρ_i meets the criteria of $2 \int_0^\infty \rho_i dz = \Sigma_i$, with 1% differences (see Appendix of Patra & Jog 2019, for detailed solving processes). Furthermore, we also calculate their 1σ errors by bootstrapping. At each bootstrap, we select a random value for each input parameter at a radius from a Gaussian distribution (the mean value is the fiducial input parameter, and the standard deviation is its uncertainty). We repeat this process 200 times and adopt the standard deviation as 1σ errors. We apply this process to all radii.

3 RESULT

By solving the equation (1), we obtain the vertical distributions of both stellar and gaseous volume densities. The convergent analytical solution is up to 6.06 kpc possibly because of faint stellar volume density beyond this radius. The results at each radius for AGC 242019 is shown in Fig. 1. We fit the stellar and gas vertical profile with $\text{sech}^2(z)$:

$$\rho_i(z) = \rho_{i,0} \times \frac{4}{\exp\left(\frac{2z}{z_0}\right) + \exp\left(\frac{-2z}{z_0}\right) + 2}, \quad (5)$$

where $\rho_{i,0}$ is volume density at mid-plane, z_0 is the dispersion. We define the scale height h_i as the half-width at half maxima (HWHM) of the vertical distribution, which gives $h_i = z_0 \log(1 + \sqrt{2})$. We further define the ratio h_i/R as the flaring angle to describe the flaring of the disk at a given radius. Since the stellar scale heights h_* depend on the adopted $\langle \sigma_z \rangle_*$, we focus only on the H I scale height h_g in this study. In addition, while sech^2 is suitable to describe the gas vertical distribution, stellar disks usually deviate from sech^2 in observations (e.g. Sarkar & Jog 2019). However, we find that the changes in h_g are small when we adopt $\text{sech}^{2/n}$ distribution for the stellar distribution (n is a free parameter to fit, and hardly deviates from 1 in our test).

For AGC 242019, the radial profiles of the H I scale height h_g and flaring angle h_g/R are shown in Fig. 2, with h_g listed in Table 1. The error bars are mostly contributed by errors of $\langle \sigma_z \rangle_g$. The mean H I scale height ($\langle h_g \rangle$) of AGC 242019 in the range of 0.67 to 6.06 kpc ($0.1R_d \sim 1.2R_d$) is 537.15 ± 89.4 pc, with standard deviation of 218.71 pc, and the mean flaring angle ($\langle h_g/R \rangle$) is 0.19 ± 0.03 , with standard deviation of 0.05. The intrinsic axis ratio can be defined

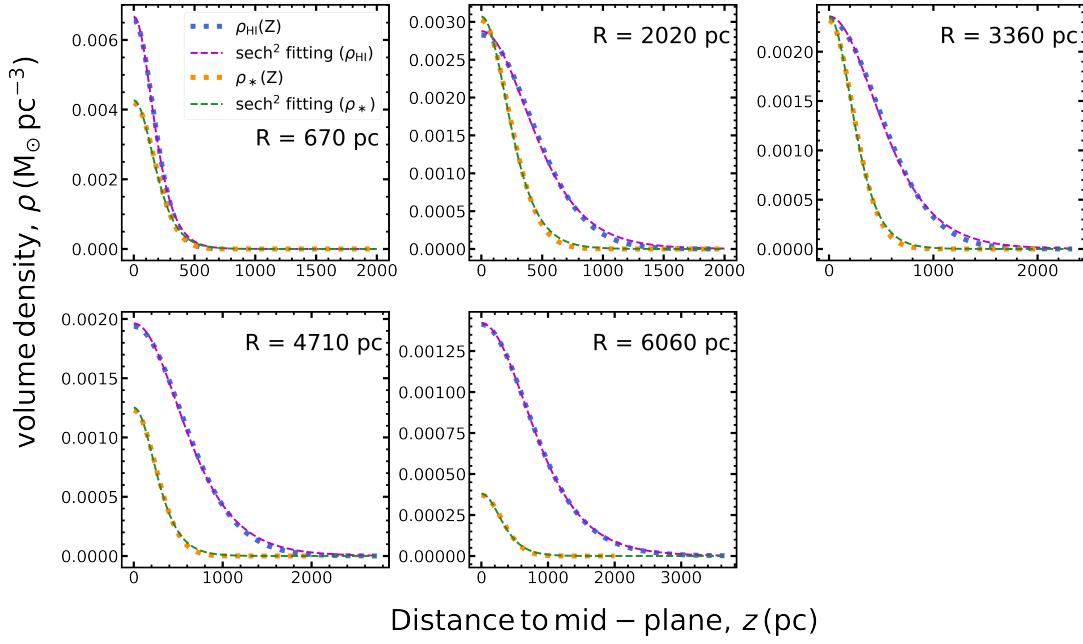


Figure 1. The derived H I and stellar vertical volume density profiles of AGC 242019 at individual radii. The blue dot lines represent derived $\rho_{\text{H I}}(z)$, and the magenta short lines represent the corresponding fit with a $\text{sech}^2(\frac{z}{z_0})$ profile. The yellow dot lines represent derived $\rho_*(z)$, and the green short lines for the fit with a $\text{sech}^2(\frac{z}{z_0})$ profile.

as $2h_{\text{g}}/R$, which gives the mean axis ratio of 0.38 ± 0.06 for AGC 242019, consistent with those of stellar disks predicted by Liao et al. (2019) and Rong et al. (2020) for isolated UDGs.

To test the influence of the adopted stellar velocity dispersion $\langle\sigma_z\rangle_*$ on the derived H I disk thickness, we use $\Delta h_{\text{g}}/h_{\text{g}} = (h'_{\text{g}} - h_{\text{g}})/h_{\text{g}}$ to quantify the fractional differences between the fiducial case (h_{g}) in § 2 and the case (h'_{g}) of different $\langle\sigma_z\rangle_*$. h'_{g} has calculated by the following cases: (i) $\langle\sigma_z\rangle_*$ varies by a factor of two; (2) $\langle\sigma_z\rangle_*$ is replaced by $\sqrt{2\pi G \Sigma_* z_e}$, $z_e = z_{0,*}/2$, where $z_{0,*}$ is what we derive previously; (3) $\langle\sigma_z\rangle_*$ is set to be equal to $\langle\sigma_z\rangle_{\text{g}}$. Fig. 3 demonstrates that the gas disk thickness is insensitive to the adopted $\langle\sigma_z\rangle_*$, with the variation less than 33%. To test the influence of the adopted dark matter profile on the H I scale height, we instead adopt the ISO model in equation (1) for AGC 242019, where the ISO model parameters are provided by Shi et al. (2021). As shown in Fig. 3, there are only less than 12% differences. We also did the above two sets of tests for dwarf irregulars, which gives similar conclusions.

The radial variation of h_{g} of each dwarf irregular is shown in Fig. A1 of Appendix A. We give the mean $\langle h_{\text{g}} \rangle$ of each dwarf irregular in the range of 0.67 to 6.06 kpc (Table 2 (7)) and $0.1R_{\text{d}}$ to $1.2R_{\text{d}}$ (Table 2 (8)) separately. In the range of 0.67 to 6.06 kpc, the mean $\langle h_{\text{g}} \rangle$ of all dwarf irregulars is around 474.76 ± 14.38 pc, with standard deviation of 216.75 pc, the mean $\langle h_{\text{g}}/R \rangle$ is around 0.2 ± 0.01 , with standard deviation of 0.09, and the mean intrinsic axis ratio is around 0.40 ± 0.01 . Our results of dwarf irregulars are consistent with previous studies (Banerjee et al. 2011; Patra 2020) that adopted Gaussian vertical distributions. The derived mean axis ratio is slightly less than that by Roychowdhury et al. (2010). The differences in h_{g} radial profiles of some dwarfs from previous studies are caused by different kinematic data. As shown in the left panels of Fig. 4, the H I scale heights and flaring angles of AGC 242019 are within the full range of dwarfs, with comparable mean values. At the given normalized radius ($0.1R_{\text{d}}$ to $1.2R_{\text{d}}$), the mean $\langle h_{\text{g}} \rangle$ of all dwarf irregulars (except DDO 54, NGC 2366, and DDO 133,

whose bar radius are larger than $1.2R_{\text{d}}$) is around 262.34 ± 11.76 pc, with a standard deviation of 138.5 pc, the mean $\langle h_{\text{g}}/R \rangle$ is around 0.37 ± 0.02 , with a standard deviation of 0.2, and the mean intrinsic axis ratio is around 0.74 ± 0.04 . As shown in the right panels of Fig. 4, the mean $\langle h_{\text{g}} \rangle$ ($\langle h_{\text{g}}/R \rangle$) of AGC 242019 is about 0.3 dexes larger (lower) than dwarf irregulars, but still in the upper (lower) bound of dwarf irregulars within 2σ (1σ) scatter. Among 14 dwarf irregulars, DDO 101 has both the lowest scale heights and flaring angles shown as an outlier of Fig. 4. This may be because dark matter, gas and stars in DDO 101 are centrally concentrated as compared to other dwarfs, which gives a steep rotation curve as well as steep radial profiles of dark matter, gas and stellar mass surface density in its inner region.

4 DISCUSSION

To further understand what drives similar scale heights between AGC 242019 and dwarf irregulars, we plot individually logarithmic parameters in equation (1) as a function of the radius normalized by R_{d} in Fig. 5: (a) the gas vertical velocity dispersion ($\langle\sigma_z\rangle_{\text{g}}$); (b) the circular velocity (v_{rot}); (c) the radial term of gravitational potential energy ($\frac{1}{R} \frac{\partial}{\partial R} (R \frac{\partial \Phi_{\text{tot}}}{\partial R})$); (d) the mass surface density of baryon ($\Sigma_{\text{baryon}} = \Sigma_* + \Sigma_{\text{gas}}$); (e) the mass surface density of dark matter ($\Sigma_{\text{DM}} = 2 \int_0^{\infty} \rho_{\text{DM}}(R, z) dz$); (f) the total mass surface density ($\Sigma_{\text{tot}} = \Sigma_{\text{baryon}} + \Sigma_{\text{DM}}$); (g) the ratio of the vertical velocity dispersion and the rotation velocity ($\langle\sigma_z\rangle_{\text{g}}/v_{\text{rot}}$) that determines the turbulent motions relative to regular motions; (h) $\langle\sigma_z\rangle_{\text{g}}^2/G\Sigma_{\text{baryon}}$ that describes the balance between pressure and the gravity of baryons; (i) $\langle\sigma_z\rangle_{\text{g}}^2/G\Sigma_{\text{tot}}$ that describes the balance between pressure and the total gravity.

AGC 242019 has comparable gas vertical velocity dispersion, circular velocity and the ratio of the two as dwarf irregulars, as shown in Fig. 5 (a), (b) and (g), respectively. The baryonic mass surface

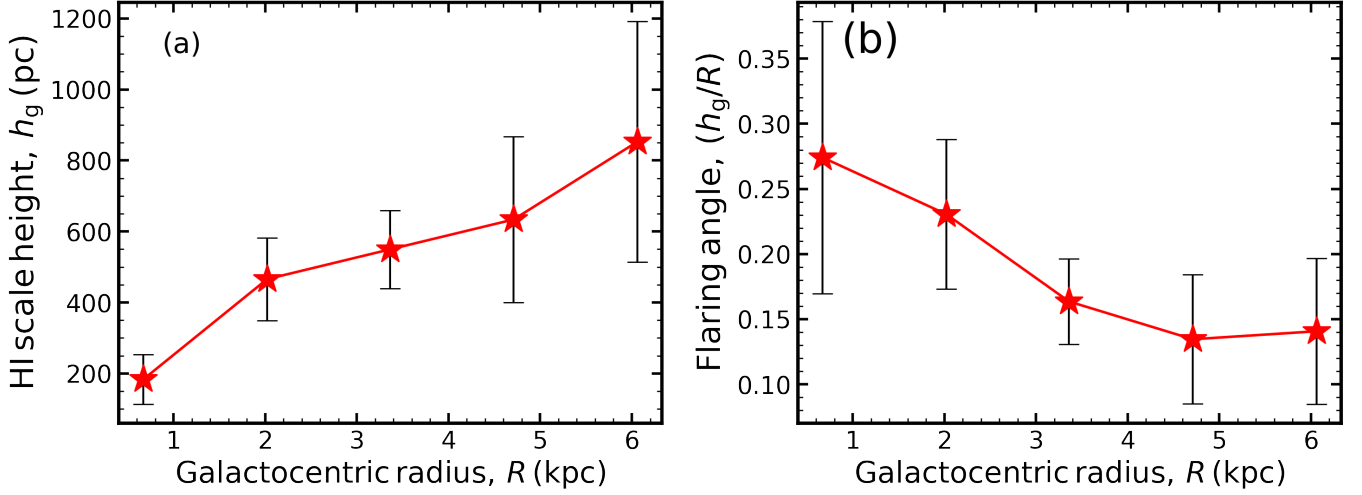


Figure 2. The H I scale heights (a) and flaring angle (b) of AGC 242019.

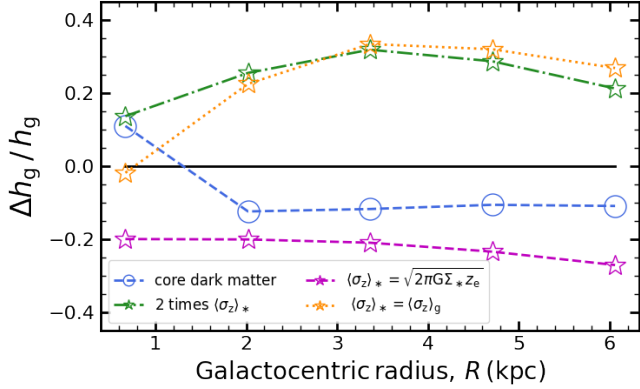


Figure 3. Differences in the gas disk scale height caused by varying the adopted stellar vertical velocity dispersion $\langle \sigma_z \rangle_*$ and dark matter profile. Δh_g is the difference between the h_g (with fiducial input parameters) and h'_g (with different input parameters). The blue circle and dot line represents the case with a ISO dark matter profile. The forest green star and dot-dash line represent the case by doubling the $\langle \sigma_z \rangle_*$. The magenta stars and dash line represents the case by adopting the $\langle \sigma_z \rangle_* = \sqrt{2\pi G \Sigma_* z_e}$, where $z_e = z_{0,*}/2$ is the half of the $\text{sech}^2(z/z_0)$ dispersion after solving equation 1. The orange stars and dot line represents the case by adopting $\langle \sigma_z \rangle_* = \langle \sigma_z \rangle_g$.

density, the dark matter mass surface density and the sum of the two of AGC 242019 is lower than the majority of dwarf irregulars as shown in Fig. 5 (d), (e) and (f), respectively. The radial gravitational potential is obviously lower than dwarf irregulars too as shown in Fig. 5 (c). The low radial gravitational potential reflects a slowly rising rotation curve, as a result of low mass surface densities. From Fig. 5 (h) and (i), the balance between turbulence and gravity of AGC 242019 is still within the range of dwarf irregulars. In fact, $h_g \propto \langle \sigma_z \rangle_g^2 / G \Sigma$ is a simplified form of hydrostatic equilibrium whose coefficients depend on the adopted disk models (e.g. van der Kruit & Searle 1981a,b; van der Kruit 1981, 1988; Bottema 1993; Kregel et al. 2002; Benítez-Llambay et al. 2018; Wilson et al. 2019; Das et al. 2020). From Fig. 5 (h) to Fig. 5 (i), AGC 242019 relative to dwarf irregulars have slight increase in $\langle \sigma_z \rangle_g^2 / G \Sigma$ after including

dark matter in Σ , implying the insignificance of dark matter in AGC 242019 relative to that in dwarfs.

By combining all objects together, we find that h_g/R is related with $\langle \sigma_z \rangle_g / v_{\text{rot}}$ as shown in Fig. 6¹. This can be roughly derived from $h_g \propto \langle \sigma_z \rangle_g^2 / G M_{\text{dyn}}$ and $G M_{\text{dyn}} = v_c^2 / R$. At $\langle \sigma_z \rangle_g / v_{\text{rot}} > 1$ there is a large scatter, which may be caused by large uncertainties of kinematic measurements in the central regions of DDO 53 and DDO 50. In spite of these outliers, the correlation is tight with a similarity to the observed relation for stellar disks of spirals in the form of $(h_g/R)_{R=R_d} \propto \langle \sigma_z \rangle_* / v_{c,\text{max}}$ (e.g. Bottema 1993; Kregel et al. 2002; Kaufmann et al. 2007; Sánchez-Janssen et al. 2010). This implies a similar origin of the flaring of gaseous disks to that of stellar disks, which is the hydrostatic equilibrium under self gravity.

AGC 242019 and dwarf irregulars are isolated systems so that their disk thickness is not likely caused by environmental effects, although some dwarfs show faint tidal tails (i.e. Hunter & Elmegreen 2006; Zhang et al. 2012). On the other hand, the stellar feedback is found to be important for dwarf galaxies: Hunter et al. (1993) found that NGC 2366, DDO 50, and DDO 53 have shell structures; Egorov et al. (2021) identified six expanding superbubbles in DDO 53; DDO 50 contains many H I holes (Puche et al. 1992; Iorio et al. 2017); Zhang et al. (2012) derived star formation histories (SFH) with the SED fitting method and found that most of them have went through active star formation phases. Stellar feedback is also proposed to be important to expand the disk sizes for H I-bearing UDGs (Jiang et al. 2019; Liao et al. 2019), which could thicken the disk as well (Sánchez-Janssen et al. 2010; Di Cintio et al. 2017; Jiang et al. 2019; Liao et al. 2019). This study indicates that AGC 242019 has a H I scale height comparable to dwarf irregulars. This implies that AGC 242019 should not experience much stronger feedback than dwarf galaxies. This is consistent with other evidences as found in Shi et al. (2021).

¹ Fitting with package LtsFit (Cappellari et al. 2013).

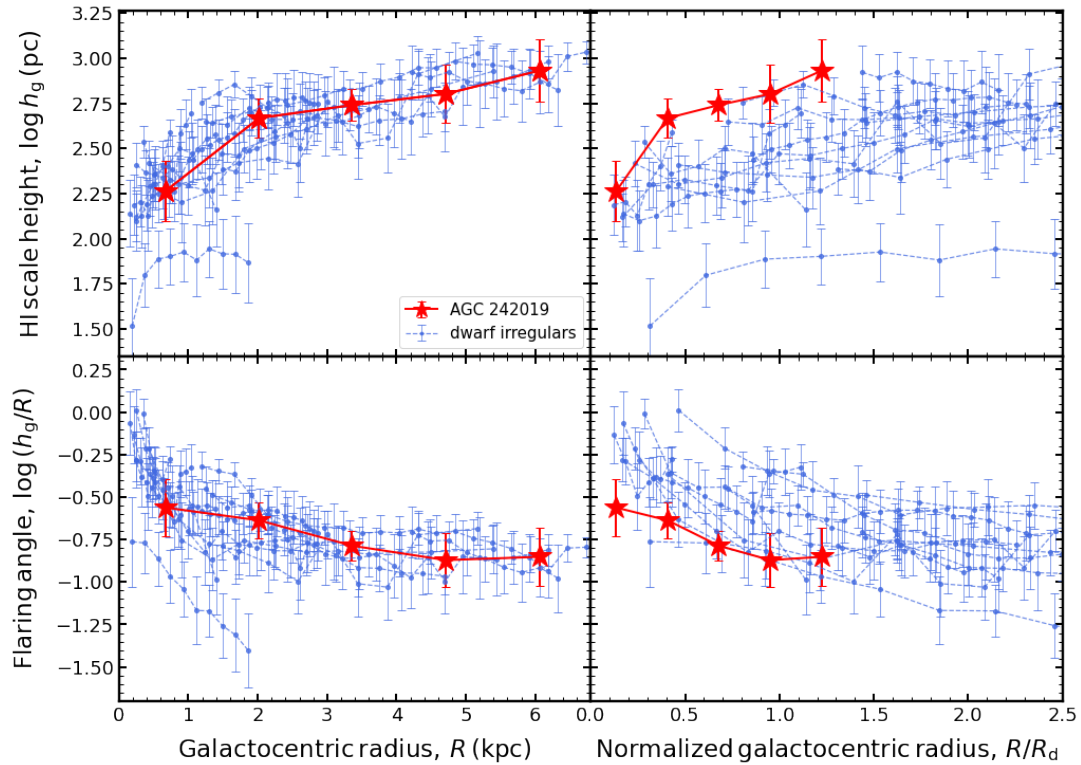


Figure 4. The H I scale height (up) and flaring angle (down) of AGC 242019 as compared to those of dwarf irregulars. The left panels are the scale height (h_g) and flaring angle (h_g/R) as a function of the physical radius, while the right panels are as a function of the normalized radius R/R_d . The red stars and solid lines represent AGC 242019, and the small blue dots and dash lines represent dwarf irregulars.

5 CONCLUSION

In this study, we derive the radial profiles of H I scale height and flaring angle of AGC 242019 and a sample of 14 dwarf irregulars for comparison. We model a galaxy as a two-component isothermal and axisymmetric disk in a dark matter halo. Assuming a self-gravitating system in hydrostatic equilibrium, we solve the joint Poisson-Boltzmann equation to estimate the gas density vertical distribution, and define the HWHM of the $\text{sech}^2(\frac{z}{z_0})$ vertical profile as the H I scale height:

(1) In the range of 0.67 to 6.06 kpc ($0.1R_d$ to $1.2R_d$), AGC 242019 has a mean H I disk scale height of 537.15 ± 89.4 pc and a mean flaring angle of 0.19 ± 0.03 . They are comparable to those of 14 dwarf irregulars in the same physical radial range. However, in the range of $0.1R_d$ to $1.2R_d$, the mean H I disk scale height of AGC 242019 is 0.3 dex larger, and the mean flaring angle is 0.3 dexes smaller than the dwarf irregulars, but still in the upper (2σ) and lower (1σ) bound of dwarf irregulars, respectively.

(2) The H I disk height of AGC 242019 is overall within the range of dwarf irregulars. This implies that AGC 242019 unlikely has experienced much stronger feedback than dwarf irregulars.

(3) The H I disks of AGC 242019 and dwarf irregulars follow a relation of $\log(h_g/R) = (0.977 \pm 0.064)(\log(\langle\sigma_z\rangle_g/v_c) + 0.666) - (0.713 \pm 0.013)$ with standard deviation of 0.10 dex.

ACKNOWLEDGEMENTS

We thank the referee for helpful and constructive comments that improved the paper significantly. XL and YS acknowledges the

support from the National Key R & D Program of China (No. 2018YFA0404502, No. 2017YFA0402704), the National Natural Science Foundation of China (NSFC grants 11825302, 12141301, 12121003, 11733002), and the China Manned Space Project with NO. CMS-CSST-2021-B02. YS thanks the Tencent Foundation through the XPLOER PRIZE.

DATA AVAILABILITY

The data underlying this article are available in the article.

REFERENCES

- Bacchini C., Fraternali F., Iorio G., Pezzulli G., Marasco A., Nipoti C., 2020, *A&A*, **641**, A70
- Banerjee A., Jog C. J., 2013, *MNRAS*, **431**, 582
- Banerjee A., Jog C. J., Brinks E., Bagetakos I., 2011, *MNRAS*, **415**, 687
- Begeman K. G., 1989, *A&A*, **223**, 47
- Begeman K. G., Broeils A. H., Sanders R. H., 1991, *MNRAS*, **249**, 523
- Benítez-Llambay A., Navarro J. F., Frenk C. S., Ludlow A. D., 2018, *MNRAS*, **473**, 1019
- Bottema R., 1993, *A&A*, **275**, 16
- Brandt J. C., 1960, *ApJ*, **131**, 293
- Burkert A., 2017, *ApJ*, **838**, 93
- Cappellari M., et al., 2013, *MNRAS*, **432**, 1709
- Chan T. K., Kereš D., Wetzel A., Hopkins P. F., Faucher-Giguère C. A., El-Badry K., Garrison-Kimmel S., Boylan-Kolchin M., 2018, *MNRAS*, **478**, 906
- Das M., McGaugh S. S., Ianjamasimanana R., Schombert J., Dwarakanath K. S., 2020, *ApJ*, **889**, 10

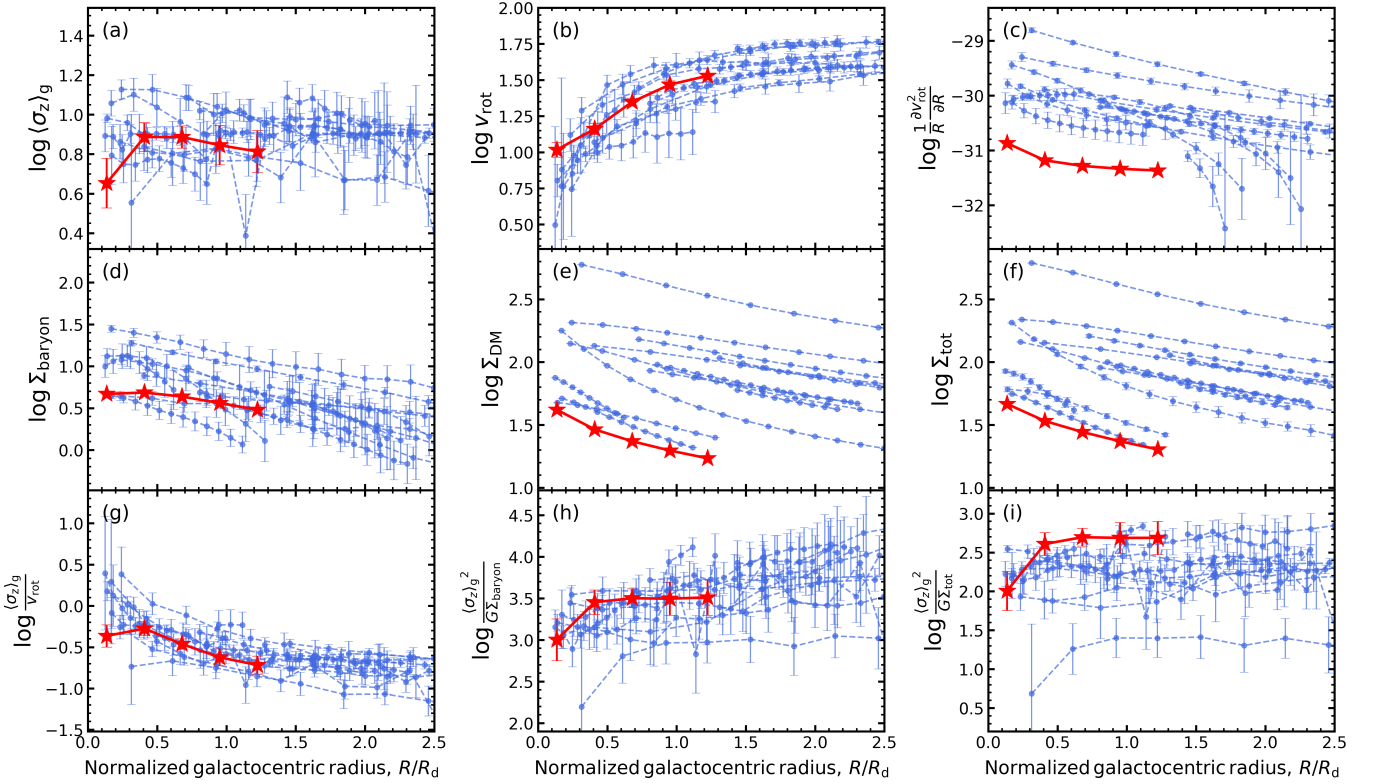


Figure 5. The physical parameters as a function of normalized radius for AGC 242019 as compared to dwarf irregulars: (a) the gas vertical velocity dispersion ($\langle\sigma_z\rangle_g$, in km/s); (b) the circular velocity (v_{rot} , in km/s); (c) the radial term of gravitational potential energy ($\frac{1}{R} \frac{\partial^2 \Phi_{\text{tot}}}{\partial R^2}$), in s^{-2}); (d) the mass surface density of baryons ($\Sigma_{\text{baryon}} = \Sigma_* + \Sigma_{\text{gas}}$, in M_{\odot}/pc^2); (e) the mass surface density of dark matter ($\Sigma_{\text{DM}} = 2 \int_0^{\infty} \rho_{\text{DM}}(R, z) dz$, in M_{\odot}/pc^2); (f) the total mass surface density ($\Sigma_{\text{tot}} = \Sigma_{\text{baryon}} + \Sigma_{\text{DM}}$, in M_{\odot}/pc^2); (g) the ratio of the vertical velocity dispersion and rotation velocity ($\langle\sigma_z\rangle_g/v_{\text{rot}}$); (h) $\langle\sigma_z\rangle_g^2/G\Sigma_{\text{baryon}}$, in pc; (i) $\langle\sigma_z\rangle_g^2/G\Sigma_{\text{tot}}$, in pc. The red stars and solid lines are AGC 242019, while the blue dots and dash lines are dwarf irregulars.

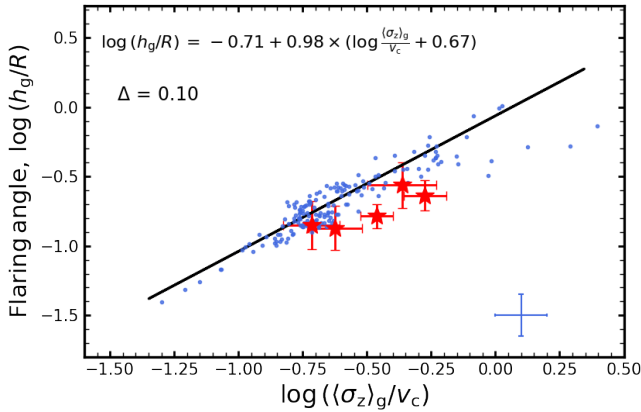


Figure 6. h_g/R versus $\langle\sigma_z\rangle_g/v_c$. The red stars are AGC 242019 and blue dots are dwarf irregulars. The median errors for dwarf irregulars are labelled in the bottom right corner of the figure. The best linear fitting is $\log(h_g/R) = (0.977 \pm 0.064) (\log(\langle\sigma_z\rangle_g/v_c) + 0.666) - (0.713 \pm 0.013)$ with standard deviation of 0.10 dex.

Di Cintio A., Brook C. B., Dutton A. A., Macciò A. V., Obreja A., Dekel A., 2017, *MNRAS*, 466, L1

Egorov O. V., Lozinskaya T. A., Vasiliev K. I., Yarovova A. D., Gerasimov I. S., Kreckel K., Moiseev A. V., 2021, *MNRAS*, 508, 2650

Graham A. W., Driver S. P., 2005, *Publ. Astron. Soc. Australia*, 22, 118
 Hunter D. A., Elmegreen B. G., 2006, *ApJS*, 162, 49
 Hunter D. A., Hawley W. N., Gallagher John S. I., 1993, *AJ*, 106, 1797
 Hunter D. A., Elmegreen B. G., Oh S.-H., Anderson E., Nordgren T. E., Massey P., Wilsey N., Riabokin M., 2011, *AJ*, 142, 121
 Hunter D. A., et al., 2012, *AJ*, 144, 134
 Iorio G., Fraternali F., Nipoti C., Di Teodoro E., Read J. I., Battaglia G., 2017, *MNRAS*, 466, 4159
 Jiang F., Dekel A., Freundlich J., Romanowsky A. J., Dutton A. A., Macciò A. V., Di Cintio A., 2019, *MNRAS*, 487, 5272
 Johnson M. C., Hunter D., Wood S., Oh S.-H., Zhang H.-X., Herrmann K. A., Levine S. E., 2015, *AJ*, 149, 196
 Kaufmann T., Wheeler C., Bullock J. S., 2007, *MNRAS*, 382, 1187
 Kregel M., van der Kruit P. C., de Grijs R., 2002, *MNRAS*, 334, 646
 Leisman L., et al., 2017, *ApJ*, 842, 133
 Liao S., et al., 2019, *MNRAS*, 490, 5182
 Mancera Piña P. E., Fraternali F., Oosterloo T., Adams E. A. K., Oman K. A., Leisman L., 2022, *MNRAS*, 512, 3230
 Marinacci F., Grand R. J. J., Pakmor R., Springel V., Gómez F. A., Frenk C. S., White S. D. M., 2017, *MNRAS*, 466, 3859
 Narayan C. A., Jog C. J., 2002a, *A&A*, 390, L35
 Narayan C. A., Jog C. J., 2002b, *A&A*, 394, 89
 Navarro J. F., Frenk C. S., White S. D. M., 1997, *ApJ*, 490, 493
 Oh S.-H., et al., 2015, *AJ*, 149, 180
 Patra N. N., 2019, *MNRAS*, 484, 81
 Patra N. N., 2020, *MNRAS*, 495, 2867
 Patra N. N., Jog C. J., 2019, *MNRAS*, 488, 4942
 Puche D., Westpfahl D., Brinks E., Roy J.-R., 1992, *AJ*, 103, 1841

- Rong Y., et al., 2020, [ApJ](#), **899**, 78
- Roychowdhury S., Chengalur J. N., Begum A., Karachentsev I. D., 2010, [MNRAS](#), **404**, L60
- Sánchez-Janssen R., Méndez-Abreu J., Aguerri J. A. L., 2010, [MNRAS](#), **406**, L65
- Sarkar S., Jog C. J., 2019, [A&A](#), **628**, A58
- Scannapieco C., Tissera P. B., White S. D. M., Springel V., 2008, [MNRAS](#), **389**, 1137
- Shi Y., Zhang Z.-Y., Wang J., Chen J., Gu Q., Yu X., Li S., 2021, [ApJ](#), **909**, 20
- Wilson C. D., Elmegreen B. G., Bemis A., Brunetti N., 2019, [ApJ](#), **882**, 5
- Wright E. L., et al., 2010, [AJ](#), **140**, 1868
- Zhang H.-X., Hunter D. A., Elmegreen B. G., Gao Y., Schruba A., 2012, [AJ](#), **143**, 47
- van Dokkum P. G., Abraham R., Merritt A., Zhang J., Geha M., Conroy C., 2015, [ApJ](#), **798**, L45
- van Dokkum P., et al., 2016, [ApJ](#), **828**, L6
- van Dokkum P., et al., 2018, [Nature](#), **555**, 629
- van Dokkum P., Danieli S., Abraham R., Conroy C., Romanowsky A. J., 2019, [ApJ](#), **874**, L5
- van der Kruit P. C., 1981, [A&A](#), **99**, 298
- van der Kruit P. C., 1988, [A&A](#), **192**, 117
- van der Kruit P. C., Searle L., 1981a, [A&A](#), **95**, 105
- van der Kruit P. C., Searle L., 1981b, [A&A](#), **95**, 116

APPENDIX A:

This paper has been typeset from a $\text{\TeX}/\text{\LaTeX}$ file prepared by the author.

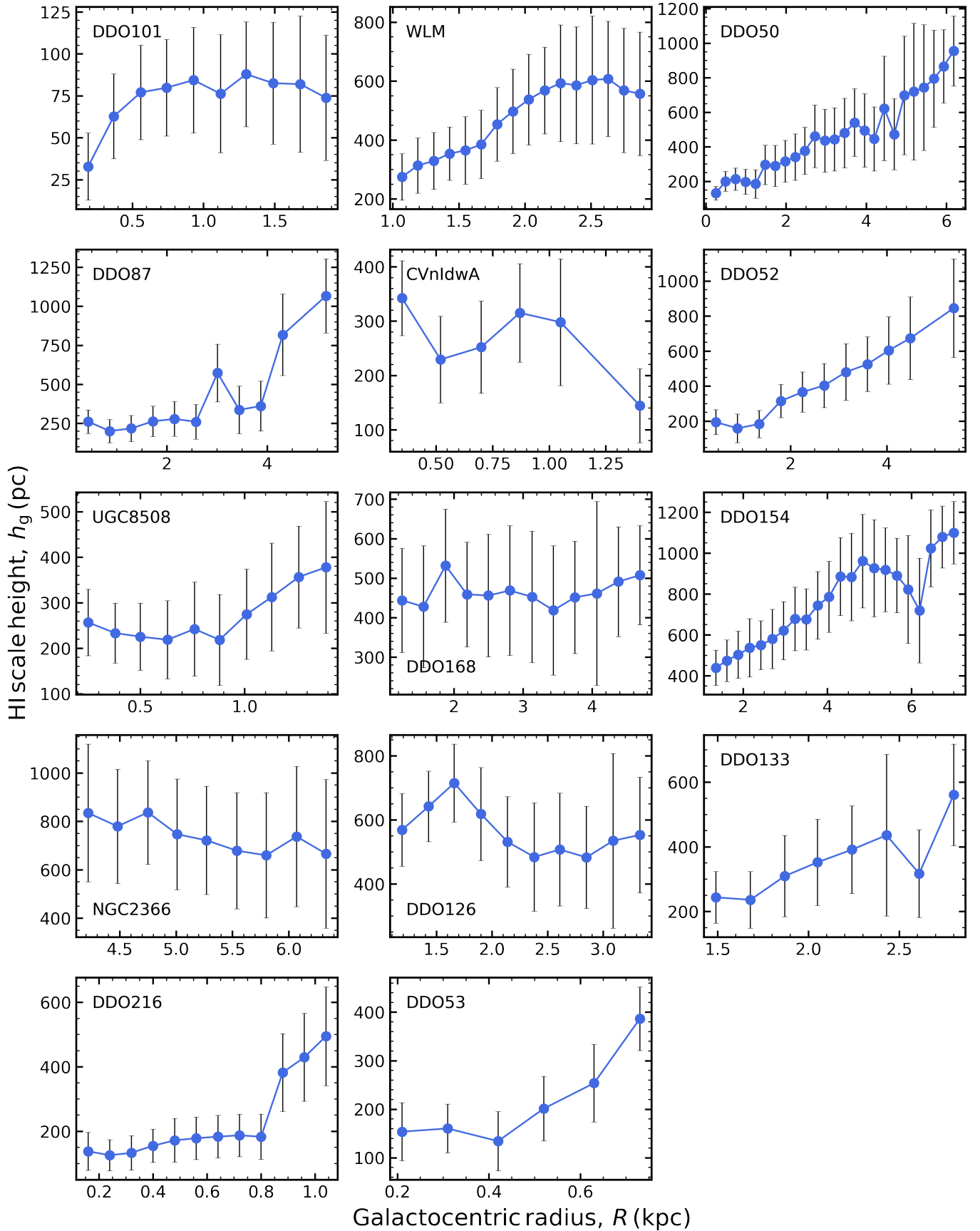


Figure A1. The H I scale heights of dwarf irregulars.